Featuring work from the Bio-NEMS/MEMS based on spintronics, Prof. Cheol Gi Kim, Daegu Gyeongbuk Institute of Science and Technology, South Korea.

Title: On-chip magnetometer for characterization of superparamagnetic nanoparticles

A μ-channel magnetometer integrated with a planar Hall magnetoresistive sensor was fabricated to measure the magnetization properties of the picoliter volume of oscillating superparamagnetic droplets.

ROYAL SOCIETY
OF CHEMISTRY

www.rsc.org/loc

On-chip magnetometer for characterization of superparamagnetic nanoparticles†

Kun Woo Kim,[a] Venu Reddy,[a] Sri Ramulu Torati,[a] Xing Hao Hu,[a] Adarsh Sandhu*[b] and Cheol Gi Kim*[a]

An on-chip magnetometer was fabricated by integrating a planar Hall magnetoresistive (PHR) sensor with microfluidic channels. The measured in-plane field sensitivities of an integrated PHR sensor with NiFe/Cu/ IrMn trilayer structure were extremely high at 8.5 μV Oe^{-1}. The PHR signals were monitored during the oscillation of 35 pL droplets of magnetic nanoparticles, and reversed profiles for the positive and negative z-fields were measured, where magnitudes increased with the applied z-field strength. The measured PHR signals for 35 pL droplets of magnetic nanoparticles versus applied z-fields showed excellent agreement with magnetization curves measured by a vibrating sample magnetometer (VSM) of 3 μL volume, where a PHR voltage of 1 μV change is equivalent to 0.309 emu cc^{-1} of the volume magnetization with a magnetic moment resolution of ~10^{-10} emu.

Introduction

Magnetic nanoparticles (MNPs) are widely used for applications in life sciences, including DNA and protein separation, drug delivery, medical imaging, and molecular diagnostics.[1–8] Notably, to maximize a functional benefit of MNPs for biomedical applications, it is critical to have a quantitative knowledge of the physical properties, such as the variation of magnetization with particle size and these nanomaterial compositions.[9–13] To date, there have been many reports on the design and synthesis of MNPs, in which the properties of the particles were evaluated after the preparation of final product. Ideally, it would be a tremendous advance in this research area if we would be able to determine the magnetic properties of ultra-small volumes of MNPs in solution with an 'on-chip' measurement system, which would enable not only the routine online monitoring of magnetic properties for quality control, but also yield new insights into the formation of the magnetic phase during the synthesis and surface functionalization.

Traditionally, vibrating sample magnetometer (VSM) and superconducting quantum interference device (SQUID)

have been used for measuring the dipole field of bulk liquid samples of over a few microliters (μL), which yields the average magnetization characteristics of the whole sample volume being studied. During VSM and SQUID measurements, the distance "d" between the sensor and the MNPs sample volume is in the order of tens of millimeters, and the dipole field from the sample magnetic moment has $1/d^3$ dependence.[14] Thus, VSM and SQUID with typical resolutions of 10^{-6} and 10^{-8} emu, respectively, are not able to measure on-chip samples with volumes of a few tens of picoliters (pL), where the magnetic moment is less than 10^{-10} emu.[15,16]

In comparison to VSM and SQUID systems, the distance "d" for an on-chip magnetometer could be reduced to a few micrometers to enable the measurement of the magnetic properties of the samples with volumes of a few tens pL due to the proximity of sensors and samples. Here, we describe the fabrication and applications of micrometer sized 'on-chip' magnetoresistive (MR) magnetic field sensors—'on-chip magnetometers'—for measuring the magnetic properties of pL volumes of MNPs. Importantly, our on-chip magnetometers were integrated with microfluidic channels to guide MNPs into close proximity to the MR sensors, which were integrated into the chips using successive hard and soft photolithographic processing. In particular, on-chip MR sensors platforms have been developed for low magnetic moment (here after magnetic field) detection; the detection of nuclear magnetic resonance (NMR) signals using anisotropic magnetoresistance (AMR) and Hall effect sensors;[17,18] detection of nanoparticle labels with giant magnetoresistance (GMR) based biochips;[19–23] and monitoring of magnetic phase transitions using planar Hall magnetoresistive (PHR) sensors.[24]

[a] Department of Emerging Materials Science, Daegu Gyeongbuk Institute of Science and Technology (DGIST), Daegu, 711-873, Republic of Korea. E-mail: cgkim@digst.ac.kr

[b] Electronics-Inspired Interdisciplinary Research Institute (EIIRIS), Toyohashi University of Technology, Hibarigaoka, Tempaku-cho, Toyohashi, 441-8580, Japan. E-mail: sandhu@eiiris.tut.ac.jp

Moreover, on-chip MR sensors have been developed for the measurement of ac-susceptibility, velocity, size monitoring, and flow rate of magnetic entities. For example, Osterberg *et al.* and Dalslet *et al.* have measured the Brownian relaxation response of magnetic nanobeads in a suspension using planar Hall effect sensors and calculated the ac-susceptibility.[25,26] Pekas *et al.* and Loureiro *et al.* integrated GMR and spin-valve sensors,[27,28] respectively, with microfluidic channels for the measurement of velocity and size monitoring, flowing height and speed of the magnetic nanoparticle droplet. However, most of the researchers focused on *M–H* magnetization curve measurement rather than susceptibility because magnetic susceptibility measured in low field region is just one of the parameter obtained from *M–H* magnetization curve, which includes the criteria on superparamagnetism, saturation field, and volume and saturation magnetism. Therefore, *M–H* curve measurement using an on-chip MR sensor has great importance; however, it is not possible to measure an *M–H* curve of the magnetic nanoparticles in the flowing mode of a droplet. Therefore, the present oscillating droplet method is the most suitable for the measurement of the *M–H* curve. In our present work, we integrated the micro valves in PDMS channel for the oscillation of the droplet, which is a very convenient way to measure an *M–H* curve, similar to the vibrating sample magnetometer.

PHR sensors have been known for their high field sensitivity, high signal-to-noise (SNR) ratio and nearly zero-offset voltage. The typical field sensitivities of cross junction PHR sensors of bilayer, trilayer and spin-valve structure are 2.5–3.0 μV Oe^{-1}, ~12 μV Oe^{-1} and 6–7 μV Oe^{-1}, respectively.[29] Therefore, the PHR sensors with trilayer structures offer the desired performance for the development of high sensitivity magnetometers. To date, reports on PHR sensor platforms for the measurement of magnetic moments of labeled MNPs with/without biomolecules have been in static platforms with the sample in close proximity to the PHR sensor.[30–32] However, for high-throughput magnetometer performance,

the magnetization of magnetic samples must be dynamically measured in the liquid phase,[33] which can be realized by the integration of microfluidic channels with PHR sensors.

We fabricated an "on-chip" ferrofluid droplet (35 pL) magnetometer with an integrated PHR sensor (Fig. 1) and measured the magnetization of superparamagnetic fluid droplets in dynamic states during both oscillation and flow. The length of the droplet was optimized such that it did not distort the peak field of the dipole moment, and the PHR signal measured was calibrated with a magnetization curve using a conventional VSM with 3 μL volume.

Materials and methods

Sensor fabrication

Chromium metal photomasks of cross-junction planar Hall magnetoresistive sensors with an active junction area of 15 μm × 15 μm and an arm length of 400 μm were designed using AutoCAD software (version 2012, Autodesk, Inc., San Rafael, CA, USA). The photomask was procured from Microimage Co. Ltd., Korea. An inverse image of the sensors was created in positive photoresist (PR) on top of a silicon wafer substrate by photolithography and exposed to ultraviolet light with a mask aligner. The cross junction sensor was stenciled on the PR layer by rinsing the silicon substrate in a developer followed rinsing by deionized water (see Fig. 1(a)).

The trilayer structure of Ta (3 nm)/NiFe (10 nm)/Cu (1.2 nm)/IrMn (10 nm)/Ta (3 nm) was sputtered onto silicon substrates by DC magnetron sputtering at a working pressure of 3 mTorr. During the sputtering process, a uniform magnetic field of 100 Oe (7.95 kA m^{-1}) was applied in plane to the film to induce uniaxial magnetic anisotropy of the ferromagnetic (FM) layer *via* exchange coupling with the antiferromagnetic (AFM) IrMn layer. This exchange coupling not only determines the sensor sensitivity, but also reduces thermal noise.
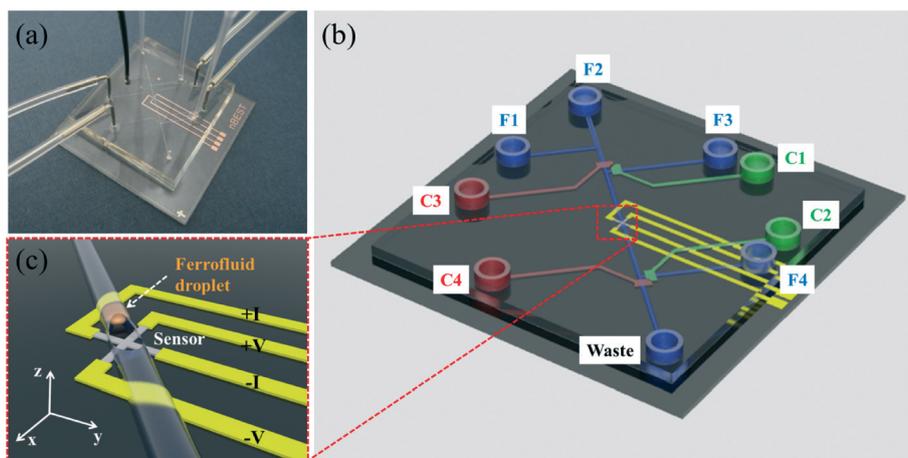

Fig. 1 (a) The on chip magnetometer. (b) Schematic drawing of on chip magnetometer, in which the channels (F1–F4) represented in blue color are flow channels for the generation of ferrofluid droplets, and the channels (C1–C4) represented in red color are control channels (valves) for the operation of ferrofluid droplet oscillation. (c) Schematic drawing of a ferrofluid droplet coming towards the PHR sensor.

The photoresistance (PR) was removed with acetone by a lift-off process, leaving the cross-junction sensor on the wafer substrate. Then, Ta (5 nm)/Au (100 nm) electrodes were fabricated by photolithography, lift-off, and DC magnetron sputtering to connect the sensor junctions with the measurement electronic circuitry. The sensor and electrodes were passivated with a SiO_2 (100 nm) layer by RF magnetron sputtering to protect the sensor junctions and electrodes from corrosion in the fluid environment.

Channel fabrication

Monolithic valves based on a PDMS stamp (Fig. 1(b)) were fabricated by multilayer soft lithography. Two PDMS membranes were used to produce crossed-channel architecture valves. Soft photolithography was used to create microchannel molds (SU-8 2025, Micro Chem) on the substrate. The first membrane was a flow channel (bottom layer) and the second membrane was a control channel (upper layer). The separation between the bottom and upper layers was ~20 μm. The height and width of the flow channels were 20 and 25 μm, respectively.

Control channel and flow channel molds were prepared using SU8-50 (Microchem, USA) and AZ4620 (MicroChem, USA) PRs, respectively. Sylgard 184 (Dow Corning, USA) compound in a 10:1 w/w ratio of base to curing agent was poured onto the "control channel" mold, transferred into a preheated oven maintained at 75 °C for 30 min, peeled from control channel, cut to the desired size and punched with holes at the end of the channels. The Sylgard 184 compound in a 20:1 w/w ratio of base to curing agent was spin coat onto the flow channel mold and transferred into a preheated oven maintained at 75 °C for 30 min. Subsequently, the punched PDMS layer of control channel was sealed on the flow channel mold using an aligning microscope, transferred into a preheated oven maintained at 75 °C for 45 min and peeled the valve containing PDMS stamp from flow channel mold. The resulting PDMS stamp was exposed to oxygen plasma and bonded with the sensor substrate using an aligning microscope. Then, the device (integrated PDMS valve and PHR sensor chip) was transferred into a preheated oven maintained at 75 °C for 45 min, cut to desired size and punched with holes at the end of the flow channels.

Generation and oscillation of ferrofluid droplets

To facilitate droplet formation, as shown in Fig. 1(c), the hydrophobic surface of the flow channel surface was modified to be hydrophilic using tetraethoxysilane (Sigma, USA). A solution of 10% tetraethoxysilane in ethanol was injected into the flow channels for 1 h, washed with ethanol and dried under vacuum. Subsequently, the flow channel F1 (Fig. 1(b)) was filled with a ferrofluid solution with volume susceptibility of 7.54 emu cc^{-1} at 100 Oe (superparamagnetic nanoparticles in oil phase, EFH Series (3–15% magnetite), Ferrotech Corporation, USA), and F2–F4 were filled with an aqueous solution phase of 50% polyethylene glycol (PEG)

(Sigma, USA) and 1% sodium dodecylsulfate (SDS) (Sigma, USA). The control channels, C1–C4, were filled with water. Droplets of ferrofluid were generated at the T-junction of the flow channels F1 and F2.

The interval and speed of droplets (500 μm s^{-1}) were regulated by adjusting air-pressure to the oil phase and the aqueous solution phase. The generated ferrofluid droplets at the T-junction of flow channels F1 and F2 were moved towards the outlet of the F2 channel by opening the control channels C1 and C2 and closing the C3 and C4 control channels. Among the many ferrofluid droplets generated in F2 channel, a single ferrofluid droplet at the sensor position was achieved by closing the control channels C1 and C2 and opening the control channels C3 and C4. Here, the sample volume was calculated to be 35 pL for a 100 μm droplet length.

In addition, the oscillation of the single ferrofluid droplet at the sensor position was achieved by consecutively applying pressure in F3 and F4 channels after closing C3 and C4. An air compressor was used to generate the pressure, which was monitored with a G49D pressure gauge (CKD, Japan). For open and close PDMS valve function, the applied pressure was regulated with a solenoid valve (Lee Co., USA).

Measurement of sensor signal

A sensing current of 1 mA was passed between the two electrodes, parallel to the uniaxial exchange anisotropy field of the trilayer structure, H_{ex}, y-direction in Fig. 1(c). The profiles of the PHR sensor signals were measured using electrodes along the x-axis under external magnetic fields ranging from −30 Oe to +30 Oe applied perpendicular to the direction of current. A uniform magnetic field was applied with perpendicular Helmholtz coils (inner diameter: 15 cm), which was controlled by a power current (HP 6643 A, USA) via the LabVIEW computer program. The magnetic field was measured by a Gaussmeter (Lakeshore 450, USA). A stage for the microfluidic chip was designed at the center of the magnetic field. A nanovoltmeter (Keithley, 2182A, USA) with the sensitivity of 10 nV was used to measure the change in voltage from the response of the oscillating magnetic droplet over the PHR sensor. The detailed experimental set up for measurement and perpendicular magnetic field application is shown in Fig. S1 (please see ESI†). All these PHR sensor characterizations were carried out at room temperature.

Finite element method simulation

A finite element method (FEM) simulation using Maxwell software (Ver. 12.2, Ansoft, USA) was carried out to determine the critical length of a droplet for an undistorted dipole field. The maximum length of the mesh was set to be 1.5 μm. The permanent magnets were introduced for the generation of a magnetic field in the magnetostatic model of the Maxwell 3d software. The measured M–H curve for 3 μL sample was used as an input parameter in Maxwell software. The M–H curve is shown in Fig. 6 (solid line). We used the measured M–H curve data for the Maxwell simulation. Field

distribution was generated by entering the M–H curve data in the Maxwell software.

Results and discussion

FEM simulation was carried out to determine the critical length of a droplet for an undistorted dipole field. The simulated results are shown in Fig. 2, where the contour flux lines of a droplet under an applied field of +100 Oe in the z-direction is shown in Fig. 2(a). The distribution of simulated B_x is plotted in Fig. 2(b) because the sensor is sensitive to the in-plane component B_x. Even though there is a

Fig. 2 (a) The contour flux lines of a droplet under an applied +100 Oe z-field. (b) The contour of B_x field. (c) The simulated profiles of various lengths of droplets, and the inset shows the critical length of droplet (above 70 μm) in which the droplet signals are apparent.

dc-offset field of earth field, the measured signal variation during the droplet oscillation is negligible because the field sensitivity of the PHR curve is linear in the range of 10 Oe. The profiles of B_x along the center line for a range of lengths of droplets are shown in Fig. 2(c). An increase in the length of a droplet leads to an increase in the peak of dipole field strength up to a droplet length of 70 μm, after which it is invariant (Fig. 2(c) and inset in Fig. 2(c)). The decrease of the peak for droplet lengths smaller than 70 μm is caused by the overlapping of positive and negative fields at the edges of the droplets. These results showed that the critical length of a droplet for undistorted field information was 70 μm for 25 μm height and 20 μm width.

For a given unidirectional anisotropy field of a sensor along the y-axis, the PHR sensor output signal is due to the x-component field. Generally, a sensor under an in-plane field in the x-axis is saturated for ~50 Oe. Initially, we used the in-plane field for the M–H curve measurement, which is shown in Fig. S2 (please see ESI†). From Fig. S2,† it is clear that the increase in voltage change by the application of the in-plane field reaches maxima around 125 Oe and it suddenly decreases. However, plotting an M–H curve for superparamagnetic nanoparticles using PHR sensor output signals requires the application of a few 100 Oe. This indicates that the in-plane measurement for the MR sensor is not suitable for the measurement of M–H curve at higher field region. Therefore, we applied the field perpendicular to the sensor (z-field) because of a higher demagnetizing field of sensor in the z-axis. The sensor signal profiles measured at several z-fields (−400, −200, 0, +200, and +400 Oe) are shown in Fig. 3(a). The resulting profiles are not equal due to the z-field effect on the magnetization of the sensing layer. Furthermore, these profiles were used to calculate the sensitivities ($S = \Delta V/\Delta H$) of the PHR sensor to be 9.5, 9.1, 8.5, 7.5, and 6.6 μV Oe^{-1} for the z-fields of −400, −200, 0, +200, and +400 Oe, respectively, and their normalized values were 1.1, 1.0, 1, 0.9, and 0.8. The fitting curve with normalized values of sensitivities is shown in Fig. 3(b). These results suggest that the signal profile and the sensitivity of the PHR sensor depend upon the sign and magnitude of the applied z-field.

Microscopic images of droplets moving forwards at several positions on the PHR sensor and their corresponding PHR signals under an applied z-field of +100 Oe are shown in Fig. 4(a). This voltage profile contains three contributions: first, as the droplet edge at the front side approaches the surface of the sensor, the voltage suddenly increases. Second, as the middle portion of the droplet approaches the surface of the sensor, the voltage nearly falls to base line. Finally, as the edge of the droplet at the back side approaches the surface of the sensor, the PHR voltage decreases. The resultant voltage profile contains two symmetric board peaks (one peak is up and another is down) and the peak between the two broad peaks is ogee-shaped (Video S1†).

This measured voltage profile is similar to the simulated voltage profile shown in Fig. 2c. The voltages for 3 cycles of oscillations are shown in Fig. 4b, where the average voltage is
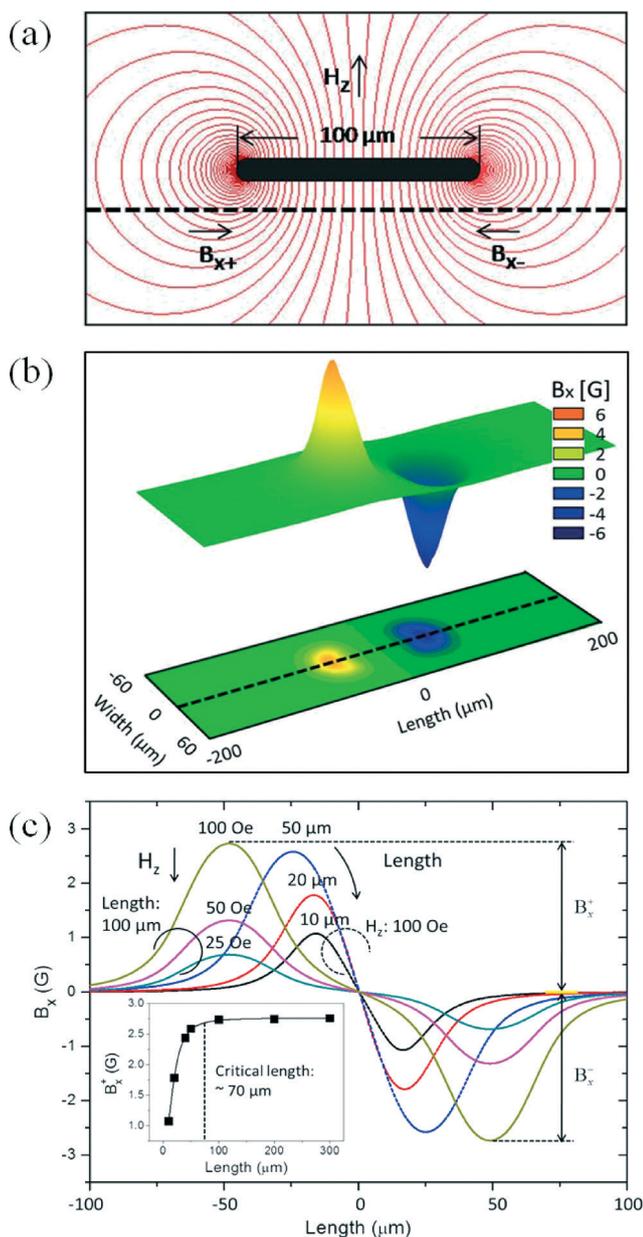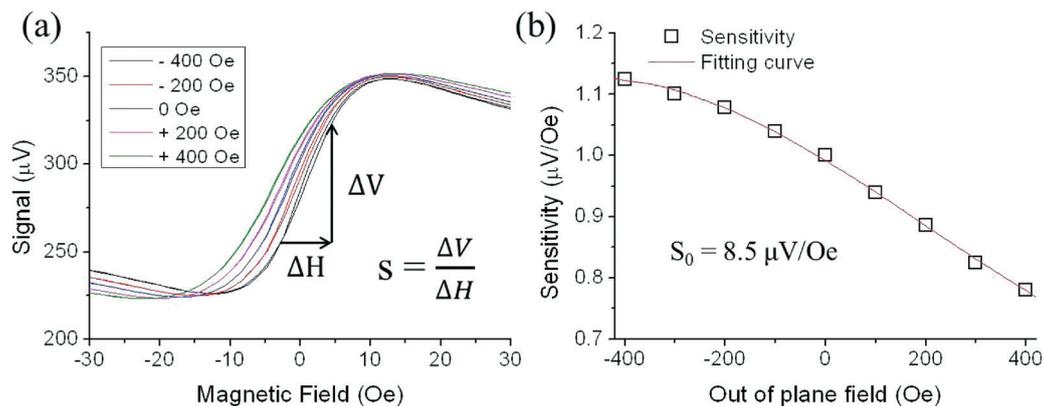
Fig. 3 (a) The sensor signal profiles are measured at various z-fields (−400, −200, 0, +200, +400 Oe). (b) Using these profiles, the sensitivities of the PHR sensor are calculated to be 9.5, 9.1, 8.5, 7.5, and 6.6; their normalized values are 1.1, 1.0, 1, 0.9, and 0.8 under z-fields at −400, −200, 0, +200, and 400 Oe, respectively.
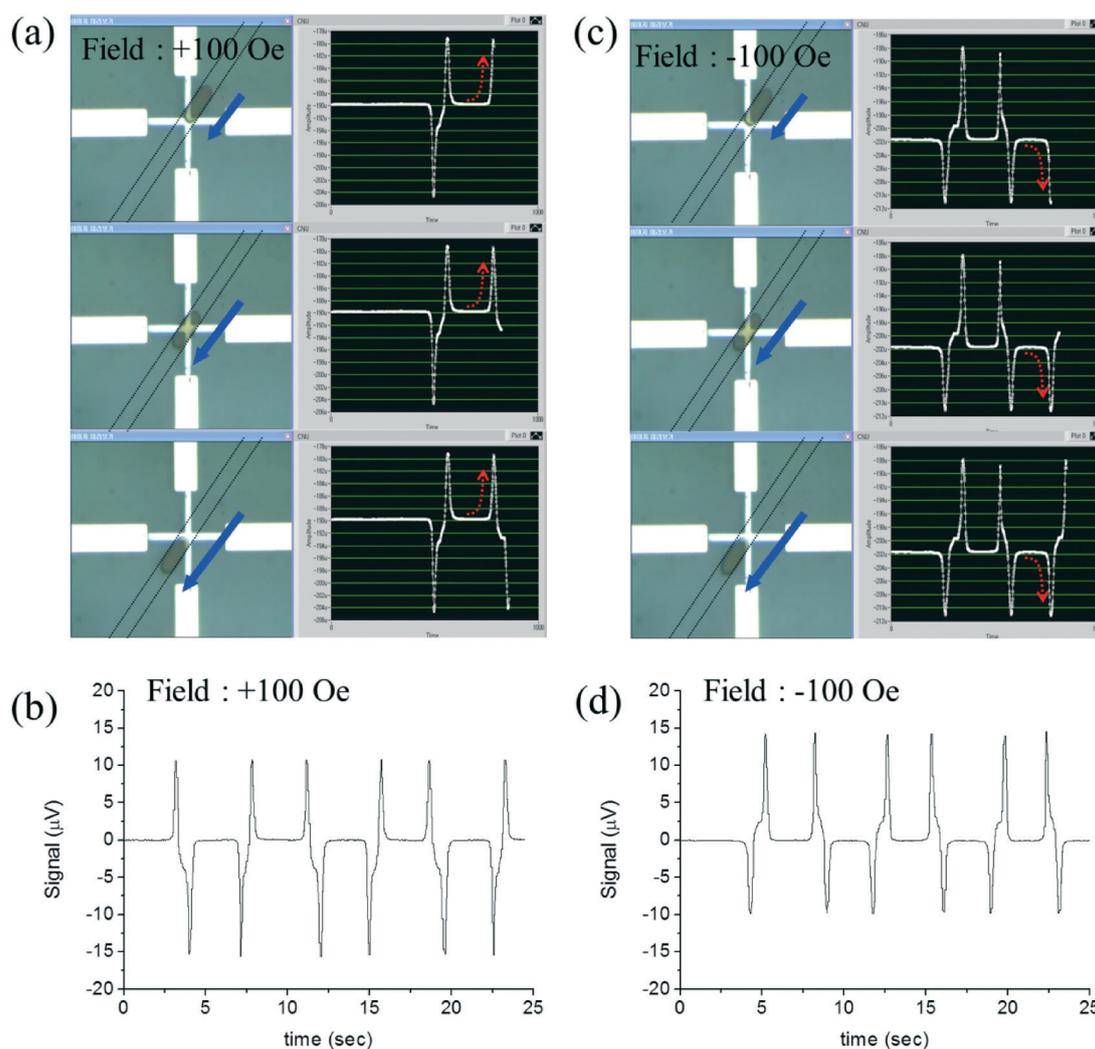

Fig. 4 (a) The microscopic images of a forward moving droplet at various positions on the PHR sensor and their corresponding measured PHR signals under +100 Oe applied z-field. (b) 3 cycles of oscillations of a forward moving droplet under +100 Oe applied z-field. (c) The microscopic images of a forward moving droplet at various positions on the PHR sensor and their corresponding measured PHR signals under −100 Oe applied z-field. (d) 3 cycles of oscillations of a forward moving droplet under −100 Oe applied z-field.

26.1 μV with a standard deviation of 0.13 μV (0.5%). Whereas under a z-field of −100 Oe, the voltage profile from a moving a droplet was an exact reverse profile of the voltage under a z-field of +100 Oe (Fig. 4(c)–(d) and Video S2†). This is due to the reversed dipole field for opposite applied fields.

To plot a magnetization curve using the PHR voltage, we carried out additional experiments to measure the voltage profile of droplets for several oscillations (several cycles) under step-like cyclic fields from positive z-field and negative z-field, as shown in Fig. 5(a) and (b), respectively. All these profiles were placed in the order of z-field from −300 to +300 Oe, as shown in Fig. 5(c).

We calculated the voltage difference between the tip of upward peak to the tip of downward peak for each applied z-field (−300 to +300 Oe), as shown in Fig. 5(a) and (b). Then, the values ($V_{peak–peak}$) were plotted against the applied z-field from −300 to +300 Oe, which is shown in Fig. 6(a). For the calibration of PHR signals, the resultant PHR voltages curve for the 35 pL sample and VSM curve obtained from a 3 μL sample were overlapped with respect to the applied z-field, as shown in Fig. 6(a). The PHR voltages curve does not exactly overlap with that of the VSM, as shown in the inset of Fig. 6(a), but when it was corrected by the sensor sensitivity with the z-field of Fig. 3(b), the PHR voltage curve efficiently overlapped with the VSM curve. The plot obtained of the PHR signal (μV) *versus* magnetization (emu cc^{-1}) was linear (Fig. 6(b)) and slope (r) was 0.309. This indicates that a change of 1 μV PHR signal is equivalent to 0.309 emu cc^{-1} of the volume magnetization with the magnetic moment resolution of ~10^{-10} emu.

For comparison with VSM measurements, the droplet volume of 35 pL was captured by closing the end of the channel. We did not observe a peak in VSM or SQUID measurements (Fig. S3†). However, there is a significant signal change in our on-chip magnetometer. The distance between the droplet and sensor surface was ~5 μm (half of the channel height) and the microfluidic channel magnetometer had signal gain of 10^9 (cm per 10 μm)^3 due to the advantage of sample proximity to sensor, compared with a conventional VSM. In a conventional VSM, the distance between the samples and sensor surface is a few tens of millimeters, which reduces the sensitivity of the system. Moreover, VSM measurements require at least a few μL of sample volume to detect a signal. The presented on-chip magnetometer is integrated with microfluidic channels, which guide the samples to close proximity of the sensor surface, a clear advantage over the conventional VSM systems. Another advantage of on-chip magnetometry includes the usage of a small volume of sample and the cost-effectiveness over conventional magnetometers. Moreover, the measurement of a liquid sample in small volume through VSM and SQUID gives noise due to vibration of the sample. Thus, VSM and SQUID systems are used for the measurement of dry samples rather than liquid sample.

The PHR voltages under different fields were measured as a function of ferrofluid droplets ranging from 1% to 100%, as shown in Fig. 7(a). The microscopic images of 1% and
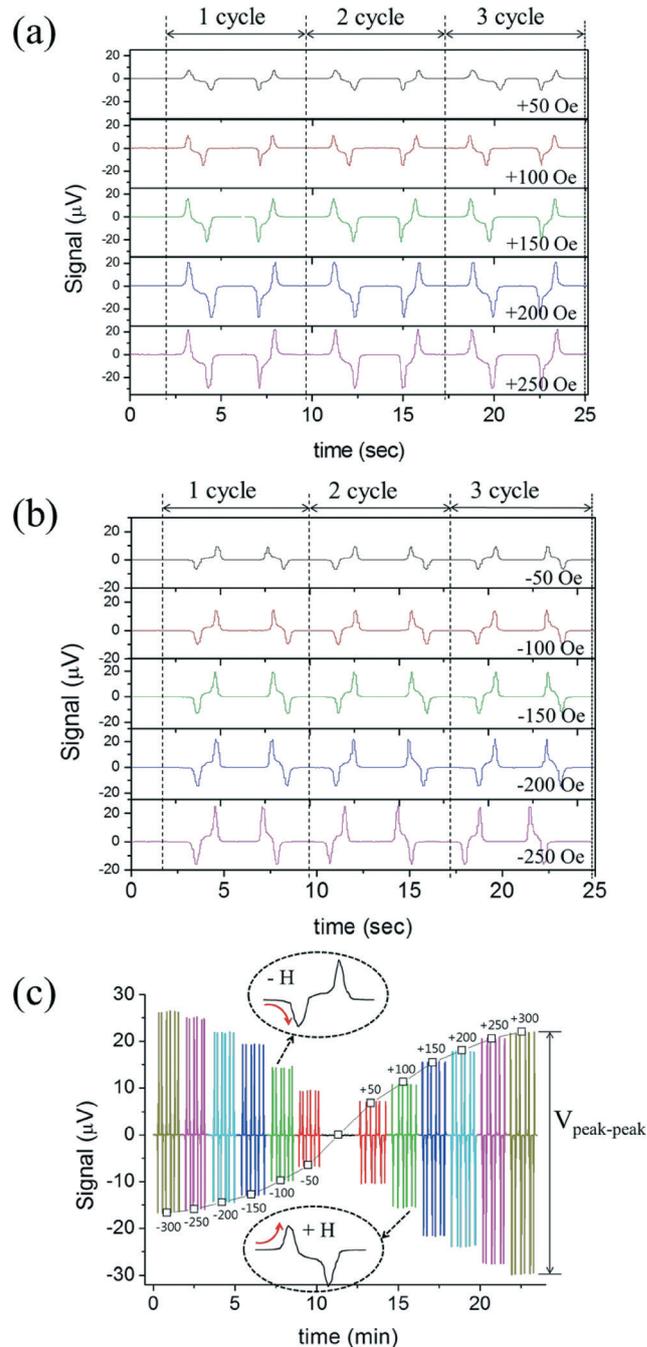

Fig. 5 (a) The voltage profile of 3 oscillations of a droplet under +50, +100, +150, +200, +250 and +300 Oe z-fields. (b) The voltage profile of 3 oscillations of a droplet under −50, −100, −150, −200, −250 and −300 Oe z-fields. (c) The profiles are placed in an order of z-fields ranging from −300 to +300 Oe.

100% droplets are shown in ESI,† Fig. S4. The PHR voltage values increased with the concentrations of ferrofluid droplets. This was due to the increase of dipole fields owing to the increased volume magnetization with both applied and ferrofluid concentrations. A fixed field of 100 Oe, a linear relationship between the ferrofluid droplet concentration (%) and magnetization (emu cc^{-1}) is shown in Fig. 7(b), which
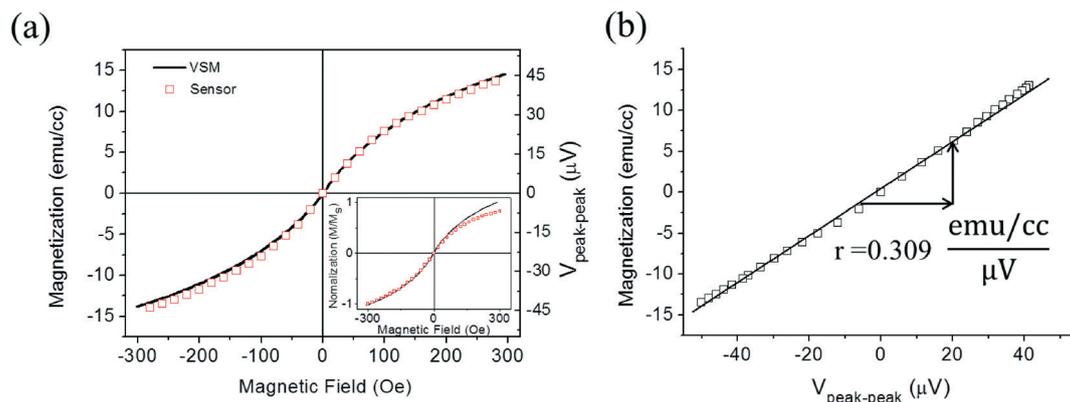
Fig. 6 (a) The overlapped graph of PHR voltages ($V_{peak-peak}$) obtained for 35 pL sample volume and VSM graph obtained from 3 μL sample volume are overlapped with respect to the applied z-field −300 to +300 Oe. The inset figure shows overlapped graph of uncorrected PHR voltages graph and VSM graph. (b) The linear plot between the PHR signal (μV) and magnetization (emu cc^{-1}).
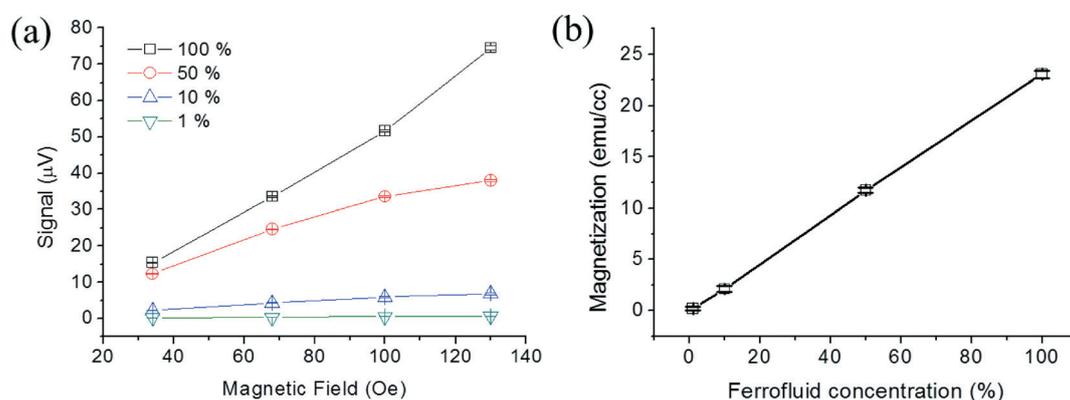

Fig. 7 (a) The PHR voltages are measured as a function of ferrofluid droplets concentrations ranging from 1% to 100%. (b) Linear relationship between ferrofluid droplets concentration (%) and magnetization (emu cc^{-1}).

confirm that the signal of the on-chip magnetometer are well defined by the magnitude of the volume magnetization.

Conclusions

An on-chip magnetometer was fabricated by integrating a PHR sensor with microfluidic channels, where the in-plane field sensitivities of the PHR sensor with Ta (3 nm)/NiFe (10 nm)/Cu (1.2 nm)/IrMn (10 nm)/Ta (3 nm) structure were 9.5, 9.1, 8.5, 7.5, and 6.6 μV Oe^{-1} for the magnetizing fields of −400, −200, 0, +200, and +400 Oe in z-direction, respectively. The critical length of droplet was determined to be 70 μm by the FEM simulation using Maxwell software for an undistorted dipole field. The monitored PHR signals during the oscillation of MNPs droplet of 35 pL showed reversed profiles for positive and negative z-fields, and their magnitudes increased with applied z-field strength. The measured PHR signals *versus* applied z-fields fitted well with $M–H$ curves measured by a vibrating sample magnetometer, and a PHR voltage of 1 μV was determined to be equivalent to 0.309 emu cc^{-1} volume magnetization. On-chip magnetic measurements for a small sample volume (35 pL) is promising for online monitoring of magnetic properties for quality control and basic understanding of magnetic phase formation during the synthesis and functionalization of superparamagnetic nanoparticles.

Acknowledgements

References

1 A. Sandhu, *Nat. Nanotechnol.*, 2007, **2**, 746–748.
2 A. M. Sandhu, M. Abe and H. Handa, *Nanotechnology*, 2011, **21**, 442001.
3 T. Y. Liu, S. H. Hu, D. M. Liu, S. Y. Chen and I. W. Chen, *Nano Today*, 2009, **4**, 52–65.
4 J. Gao, H. Gu and B. Xu, *Acc. Chem. Res.*, 2009, **42**, 1097–1107.
5 A. Ranzoni, G. SabattevanI, L. J. Jzendoorn and M. W. J. Prins, *ACS Nano*, 2012, **6**, 3134–3141.

6   J. C. Frias, Y. Ma, K. J. Williams, Z. A. Fayad and E. A. Fisher, *Nano Lett.*, 2006, **6**, 2220–2224.

7   J.-H. Lee, J. T. Jang, J. S. Choi, S. H. Moon, S. H. Noh, J. W. Kim, J. G. Kim, I. S. Kim, K. I. Park and J. Cheon, *Nat. Nanotechnol.*, 2011, **6**, 418–422.

8   D. M. Bruls, T. H. Evers, J. A. H. Kahlman, P. J. W. van Lankvelt, M. Ovsyanko, E. G. M. Pelssers, J. J. H. B. Schleipen, F. K. de Theije, C. A. Verschuren, T. van der Wijk, J. B. A. van Zon, W. U. Dittmer, A. H. J. Immink, J. H. Nieuwenhuis and M. W. J. Prins, *Lab Chip*, 2009, **9**, 3504–3510.

9   A. K. Gupta and M. Gupta, *Biomaterials*, 2005, **26**, 3995–4021.

10 O. V. Salata, *J. Nanobiotechnol.*, 2004, **2**, 3.

11 I. Mönch, A. Meye, A. Leonhardt, K. Krämer, R. Kozhuharova, T. Gemming, M. P. Wirth and B. Büchner, *J. Magn. Magn. Mater.*, 2005, **290**, 276–278.

12 S. T. Reddy, A. J. Van der Vlies, E. Simeoni, V. Angeli, G. J. Randolph, C. P. O'Neil, L. K. Lee, M. A. Swartz and J. A. Hubbell, *Nat. Biotechnol.*, 2007, **25**, 1159–1164.

13 D. Bechet, P. Couleaud, C. Frochot, M. Viriot, F. Guillemin and M. Barberi-Heyob, *Trends Biotechnol.*, 2008, **26**, 612–621.

14 R. C. O'Handley, *Modern Magnetic Materials: Principles and Applications*, Wiley, New York Chichester, 1999, p. 52.

15 S. Foner, *Rev. Sci. Instrum.*, 1959, **30**, 548–557.

16 D. Drung, C. Assmann, J. Beyer, A. Kirste, M. Peters, F. Ruede and T. Sching, *IEEE Trans. Appl. Supercond.*, 2007, **17**, 699–704.

17 F. Verpillat, M. P. Ledbetter, S. Xu, D. J. Michalak, C. Hilty, L.-S. Bouchard, S. Antonijevic, D. Budker and A. Pines, *Proc. Natl. Acad. Sci. U. S. A.*, 2008, **105**, 2271–2273.

18 G. Boero, P. A. Besse and R. Popovic, *Appl. Phys. Lett.*, 2001, **79**, 1498–1500.

19 D. R. Baselt, G. U. Lee, M. Natesan, S. W. Metzger, P. E. Sheehan and R. J. A. Colton, *Biosens. Bioelectron.*, 1998, **13**, 731–739.

20 *Magnetoelectronics*, ed. P. P. Freitas, H. A. Ferreira, D. L. Graham, L. A. Clarke, M. D. Amaral, V. Martins, L. Fonseca, J. S. Cabral and M. Johnson, Elsevier Amsterdam, 2004, ch. 7.

21 S. J. Osterfeld, H. Yu, R. S. Gaster, S. Caramuta, L. Xu, S. J. Han, D. A. Hall, R. J. Wilson, S. Sun, R. L. White, R. W. Davis, N. Pourmand and S. X. Wang, *Proc. Natl. Acad. Sci. U. S. A.*, 2008, **105**, 20637–20640.

22 R. S. Gaster, L. Xu, S. J. Han, R. J. Wilson, D. A. Hall, S. J. Osterfeld, H. Yu and S. X. Wang, *Nat. Nanotechnol.*, 2011, **6**, 314–320.

23 B. Srinivasan, Y. Li, Y. Jing, Y. Xu, X. Yao, C. Xing and J. P. Wang, *Angew. Chem., Int. Ed.*, 2009, **48**, 2764–2767.

24 T. Q. Hung, F. Terki, S. Kamara, M. Dehbaoui, S. Charar, B. Sinha, C. G. Kim, P. Gandit, I. A. Guralskiy, G. Molnar, L. Salmon, H. J. Shepherd and A. Bousseksou, *Angew. Chem., Int. Ed.*, 2013, **52**, 1185–1188.

25 F. W. Osterberg, G. Rizzi, T. Zardán Gómez delaTorre, M. Stromberg, M. Stromme, P. Svedlindh and M. F. Hansen, *Biosens. Bioelectron.*, 2013, **40**, 147–152.

26 B. T. Dalslet, C. D. Damsgaard, M. Donolato, M. Strømme, M. Stromberg, P. Svedlindh and M. F. Hansen, *Lab Chip*, 2010, **11**, 296–302.

27 N. Pekas, M. Tondra, A. Popple, A. Jander and M. D. Porter, *Appl. Phys. Lett.*, 2004, **85**, 4783–4785.

28 J. Loureiro, R. Ferreira, S. Cardoso, P. P. Freitas, J. Germano, C. Fermon, G. Arrias, M. Pannetier-Lecoeur, F. Rivadulla and J. Rivas, *Appl. Phys. Lett.*, 2009, **95**, 034104.

29 B. Sinha, T. Q. Hung, T. S. Ramulu, S. Oh, K. Kim, D. Y. Kim, F. Terki and C. G. Kim, *J. Appl. Phys.*, 2013, **113**, 063903.

30 S. Oh, M. Jadhav, J. Lim, V. Reddy and C. G. Kim, *Biosens. Bioelectron.*, 2013, **41**, 758–763.

31 B. Sinha, T. S. Ramulu, K. W. Kim, R. Venu, J. J. Lee and C. G. Kim, *Biosens. Bioelectron.*, 2014, **59**, 140–144.

32 B. Sinha, S. Anandakumar, S. Oh and C. G. Kim, *Sens. Actuators, A*, 2012, **182**, 34–40.

33 I. Monch, D. Makarov, R. Koseva, L. Baraban, D. Karnaushenko, C. Kaiser, K. F. Arndt and O. G. Schmidt, *ACS Nano*, 2011, **5**, 7436–7442.